

A multilevel fast multipole based approach for efficient reconstruction of perfectly conducting scatterers

Michael Brandfass and Weng Cho Chew

This work was supported by DARPA under Contract F49620-98-1-0498.

Dept. Elec. & Comp. Eng., University of Illinois, Urbana, IL 61801-2991, USA (e-mail: michael@sunchew.ece.uiuc.edu)

Abstract

A nonlinear reconstruction scheme based on the Distorted Born Iterative Method (DBIM) is presented to solve two-dimensional inverse scattering problems with metallic scatterers. Half-quadratic regularization alleviates the inherently ill-posed problem of nonlinear inverse scattering while simultaneously preserving edges. Reconstruction results are found by minimizing a cost function.

A bistatic experimental set-up is studied with angular and frequency diversity. A Multilevel Fast Multipole Algorithm (MLFMA) combined with a conjugate gradient (CG) scheme is introduced to solve the forward as well as the inverse scattering problem involved in the DBIM. The computational complexity per CG iteration using the MLFMA is of order $\mathcal{O}(N \log N)$ compared to $\mathcal{O}(N^2)$ in a standard implementation without the MLFMA.

Numerical reconstruction results obtained from synthetic scattering data are presented.

Keywords

Distorted Born Iteration Method, Multilevel Fast Multipole Algorithm, nonlinear inverse scattering, edge-preserving regularization

INTRODUCTION

Most SAR imaging schemes linearize the inverse scattering problem by defining a reflectivity function which is independent of the total field distribution on or within the scatterer. These schemes implicitly introduce linearizing approximations (such as Born or Kirchhoff) and ignore multiple interactions between the scatterer and the scattered field. Hence, radar imaging of rigid scatterers such as conducting aircraft suffers if multiple reflections occur. The Distorted Born inversion Method (DBIM) accounts for nonlinear effects and does not introduce any linearizing approximations. The solution is found by iteratively minimizing a cost function [5], [6], [1], [2]. This cost function compares the measured scattered field with the computed scattered field, obtained from the last scatterer reconstruction update.

Several reconstruction approaches have been suggested in the literature to reconstruct conducting scatterers. In most of the suggested schemes, Fourier descriptors were used to parameterize the reconstruction models [1], [4], [3]. In [2] a polygonal parameterization was used. These discretizations have the disadvantage that *a priori* knowledge of the number of scatterers in the reconstruction domain is necessary. Furthermore, for all the schemes using Fourier descriptors, the coordinate system's origin has to be either within the scatterer domain or the distance between the origin and a point within the scatterer domain has to be known to ensure uniqueness of the scatterer's describing radial parameter in the polar-coordinate system. With the scheme suggested in this paper multiple

scatterers can be reconstructed without changing the underlying equations (as necessary in [3]) and without *a priori* knowledge of the number of scatterers.

A bistatic set-up with either angular diversity or both angular and frequency diversity is assumed. For numerical implementation of the DBIM, the forward problem needs to be solved for all the excitation frequencies and angles of the incident fields for each scatterer update. The computational complexity and the storage requirement needed to solve the forward problem, discretized by N subscatterers, via an iterative solver (e.g. conjugate gradient method) is of order $\mathcal{O}(N^2)$ per iteration. To speed up the computation, the Multilevel Fast Multipole Algorithm (MLFMA) [7], [8] is introduced to solve the forward as well as the inverse problem. Solving the “inverse problem” in a DBIM iteration implies that we trace a small change in data to a small change in the scatterer. This small change in the scatterer is computed via a conjugate-gradient scheme. Storage and CPU requirements of the MLFMA solver are of $\mathcal{O}(N \log N)$ for each conjugate-gradient iteration. The MLFMA recursively subdivides the reconstruction domain into a tree construction and aggregates the divided subscatterers from the finest to the coarsest level. We also apply this multilevel fast multipole principle to the inverse solver by making use of an asymmetric multiple tree structure, specially adapted to DBIM and the case where the source and observation points do not coincide with each other. Through the additional use of MLFMA for the inverse solver, the overall computational complexity remains at $\mathcal{O}(N \log N)$. To the author’s knowledge, this is the first journal paper dealing with the Multilevel Fast Multipole Algorithm adapted to DBIM to numerically accelerate a nonlinear reconstruction problem. It’s results were first presented in [11].

In Section I, the electromagnetic scattering problem is derived and the resulting integral equations are discretized. Section II introduces the Distorted Born Iterative Method. The fundamentals of the MLFMA are explained in Section III. In Section IV, the half-quadratic regularization principle is summarized and the final iteration scheme is presented. Section V describes the simulated reconstruction configuration and shows reconstruction results.

I. FORMULATION OF THE SCATTERING PROBLEM

A. Integral representations for the TE-polarization

A detailed derivation of the integral representations for the two-dimensional case is given in the appendix. For the Transverse Electric (TE) polarization we can determine the scattered magnetic field on the measurement contour from the knowledge of the total magnetic field $H_z(\mathbf{R}, \omega)$ in the

reconstruction domain. We obtain from the derivation in the appendix the total magnetic field for a perfectly electric conducting scatterer:

$$H_z(\mathbf{R}, \omega) = H_z^i(\mathbf{R}, \omega) + \underbrace{\int_{\mathbf{R}' \in C} H_z(\mathbf{R}', \omega) \mathbf{n}(\mathbf{R}') \cdot \nabla' G(\mathbf{R}, \mathbf{R}', \omega) dR'}_{= H_z^s(\mathbf{R}, \omega)} \quad (1)$$

where \mathbf{R} is the observation point vector, \mathbf{n} is the outward normal vector of the scatterer, $H_z^i(\mathbf{R}, \omega)$ is the incident magnetic field and $G(\mathbf{R}, \mathbf{R}', \omega)$ is the free space two-dimensional scalar Green's function. Analogously, for the scattered magnetic field on the measurement surface, we have

$$H_z^{sM}(\mathbf{R}, \omega) = \int_{\mathbf{R}' \in C} H_z(\mathbf{R}', \omega) \mathbf{n}(\mathbf{R}') \cdot \nabla' G(\mathbf{R}, \mathbf{R}', \omega) dR' \quad (2)$$

where \mathbf{R} is the observation point on the measurement surface.

B. Integral representations for the TM-polarization

In a similar way as shown in the appendix, we can find formulas analogous to Eqs. (67) and (2) for the Transverse Magnetic (TM) polarization considering perfectly electric conducting scatterers. We want access to the components of the normal field $\mathbf{n}(\mathbf{R})$ of the scatterer rather than the current $\mathbf{J}_s(\mathbf{R})$ on the scatterer. For convenience, the derived reconstruction procedure for the TM-polarization should be formally equivalent to the TE-case. To comply with these requirements, we perform a gradient operation on the TM-polarization formulas, yielding

$$\nabla E_z^i(\mathbf{R}, \omega) = \int_{\mathbf{R}' \in C} \nabla' E_z(\mathbf{R}', \omega) \cdot (\mathbf{I}\delta(\mathbf{R} - \mathbf{R}') - \mathbf{n}(\mathbf{R}')) \nabla' G(\mathbf{R}, \mathbf{R}', \omega) dR' \quad (3)$$

and

$$\nabla E_z^{sM}(\mathbf{R}, \omega) = \int_{\mathbf{R}' \in C} \mathbf{n}(\mathbf{R}') \cdot \nabla' E_z(\mathbf{R}', \omega) \nabla' G(\mathbf{R}, \mathbf{R}', \omega) dR' . \quad (4)$$

C. Discretization of the field integral equations

The Method of Moments is used to discretize the pertinent integral equations via pulse-basis functions and point matching for testing. The numerical integration over the discretized contour elements C_w is performed by the Gauss-Legendre quadrature rule and the lengths of the integration elements C_w are chosen by the diameters of equivalently sized circles of the discretization patches in the reconstruction domain, so that the elements of the Green's matrix defined later in Eq. (10)

and Eq. (14) are given by

$$\mathbf{g}_w(\mathbf{R}_v) = \frac{jk}{4} \int_{C_w} \frac{\mathbf{R}_v - \mathbf{R}'}{|\mathbf{R}_v - \mathbf{R}'|} H_1^{(1)}(k|\mathbf{R}_v - \mathbf{R}'|) dR' \quad (5)$$

with

$$g_w^x(\mathbf{R}_v) = \mathbf{e}_x \cdot \mathbf{g}_w(\mathbf{R}_v) \quad \text{and} \quad g_w^y(\mathbf{R}_v) = \mathbf{e}_y \cdot \mathbf{g}_w(\mathbf{R}_v) \quad (6)$$

where $H_1^{(1)}$ is the Hankel function of the first kind and first order and \mathbf{R}_v is the observation point vector at the v 's position on the scatterer contour.

D. Introduction of vector and matrix notation

Equations (67) and (3) can be written in matrix notation with the Green's matrix $\overline{\mathbf{G}}_{CC}$ which consists of the vector elements of the free-space Green's function. These vector elements can be split into two components, one for the x direction and the other for the y direction, so the matrix $\overline{\mathbf{G}}_{CC}$ consists of two submatrices. Let L be the number of source/observation points on the scatterer surface. Thus, in the TM case, for the total electric field on the surface of the scatterer, it follows that

$$\mathbf{E}_C^{\nabla;[2L \times 1]} = \left(\overline{\mathbf{I}}^{[2L \times 2L]} - \overline{\mathbf{G}}_{CC}^{[2L \times L]} \cdot \overline{\mathbf{n}}^{[L \times 2L]} \right)^{-1} \cdot \mathbf{E}_{C;i}^{\nabla;[2L \times 1]} \quad \text{with} \quad (7)$$

$$\mathbf{E}_{C;i}^{\nabla;[2L \times 1]} = [\partial_x E_z^i(\mathbf{R}_1), \dots, \partial_x E_z^i(\mathbf{R}_v), \dots, \partial_x E_z^i(\mathbf{R}_L) \mid \partial_y E_z^i(\mathbf{R}_1), \dots, \partial_y E_z^i(\mathbf{R}_v), \dots, \partial_y E_z^i(\mathbf{R}_L)]^T \quad (8)$$

$$\mathbf{E}_C^{\nabla;[2L \times 1]} = [\partial_x E_z(\mathbf{R}_1), \dots, \partial_x E_z(\mathbf{R}_w), \dots, \partial_x E_z(\mathbf{R}_L) \mid \partial_y E_z(\mathbf{R}_1), \dots, \partial_y E_z(\mathbf{R}_w), \dots, \partial_y E_z(\mathbf{R}_L)]^T \quad (9)$$

$$\overline{\mathbf{n}}^{[L \times 2L]} = \begin{bmatrix} n_1^x(\mathbf{R}_1) & \dots & 0 & \mid & n_1^y(\mathbf{R}_1) & \dots & 0 \\ \vdots & \ddots & \vdots & \mid & \vdots & \ddots & \vdots \\ 0 & \dots & n_L^x(\mathbf{R}_L) & \mid & 0 & \dots & n_L^y(\mathbf{R}_L) \end{bmatrix}; \quad \overline{\mathbf{G}}_{CC}^{[2L \times L]} = \begin{bmatrix} g_1^x(\mathbf{R}_1) & \dots & g_1^x(\mathbf{R}_L) \\ \vdots & \ddots & \vdots \\ g_L^x(\mathbf{R}_1) & \dots & g_L^x(\mathbf{R}_L) \\ \text{-----} \\ g_1^y(\mathbf{R}_1) & \dots & g_1^y(\mathbf{R}_L) \\ \vdots & \ddots & \vdots \\ g_L^y(\mathbf{R}_1) & \dots & g_L^y(\mathbf{R}_L) \end{bmatrix} \quad (10)$$

For the total magnetic field in the TE case, it follows that:

$$\mathbf{H}_C^{[L \times 1]} = \left(\overline{\mathbf{I}}^{[L \times L]} - \overline{\mathbf{G}}_{CC}^{[L \times 2L]} \cdot \overline{\mathbf{n}}^{[2L \times L]} \right)^{-1} \cdot \mathbf{H}_{C;i}^{[L \times 1]} \quad \text{where we have} \quad (11)$$

$$\mathbf{H}_{C;i}^{[L \times 1]} = [H_z^i(\mathbf{R}_1), H_z^i(\mathbf{R}_2), \dots, H_z^i(\mathbf{R}_v), \dots, H_z^i(\mathbf{R}_L)]^T \quad (12)$$

$$\mathbf{H}_C^{[L \times 1]} = [H_z(\mathbf{R}_1), H_z(\mathbf{R}_2), \dots, H_z(\mathbf{R}_w), \dots, H_z(\mathbf{R}_L)]^T \quad (13)$$

$$\overline{\mathbf{G}}_{CC}^{[L \times 2L]} = \begin{bmatrix} g_1^x(\mathbf{R}_1) \dots g_1^x(\mathbf{R}_L) & | & g_1^y(\mathbf{R}_1) \dots g_1^y(\mathbf{R}_L) \\ \vdots & \ddots & \vdots & \ddots & \vdots \\ g_L^x(\mathbf{R}_1) \dots g_L^x(\mathbf{R}_L) & | & g_L^y(\mathbf{R}_1) \dots g_L^y(\mathbf{R}_L) \end{bmatrix}; \quad \overline{\mathbf{n}}^{[2L \times L]} = \begin{bmatrix} n_1^x(\mathbf{R}_1) & \dots & 0 \\ \vdots & \ddots & \vdots \\ 0 & \dots & n_L^x(\mathbf{R}_L) \\ \hline n_1^y(\mathbf{R}_1) & \dots & 0 \\ \vdots & \ddots & \vdots \\ 0 & \dots & n_L^y(\mathbf{R}_L) \end{bmatrix} \quad (14)$$

$\overline{\mathbf{n}}$ consists of two submatrices which contain the scatterer surface normal components n_x and n_y . Both these submatrices are diagonal.

In the same manner we obtain the electric and magnetic scattered field on the measurement surface according to

$$\mathbf{E}_{Calc;s}^{\nabla;[2M \times 1]} = \overline{\mathbf{G}}_{MC}^{[2M \times L]} \cdot \overline{\mathbf{n}}^{[L \times 2L]} \cdot \mathbf{E}_C^{\nabla;[2L \times 1]} \quad (15)$$

and

$$\mathbf{H}_{Calc;s}^{[M \times 1]} = \overline{\mathbf{G}}_{MC}^{[M \times 2L]} \cdot \overline{\mathbf{n}}^{[2L \times L]} \cdot \mathbf{H}_C^{[L \times 1]} \quad (16)$$

where $\mathbf{E}_{Calc;s}^{\nabla;[2M \times 1]}$, $\mathbf{H}_{Calc;s}^{[M \times 1]}$ are the computed differential scattered electric field and the computed magnetic field on the measurement surface, respectively, and $\mathbf{E}_C^{\nabla;[2L \times 1]}$, $\mathbf{H}_C^{[L \times 1]}$ are the differential total electric and the total magnetic field on the scatterer contour. $\overline{\mathbf{G}}_{MC}$ is the Green's matrix which connects the contour of the scatterer with the measurement surface. It has the same structure as $\overline{\mathbf{G}}_{CC}$ in Eq. (14), but with the difference that the observation points are located on the measurement surface. L denotes the total number of samples on the contour of the scatterer and M denotes the number of measurement points.

II. FORMULATION OF THE INVERSE PROBLEM

A. Distorted Born Iterative Method

For the TE case, the discretized matrix equation of the scattered field (16) depends on the discretized scatterer elements in the form of the diagonal matrix $\overline{\mathbf{n}}$. We can derive the *Frechet*-derivative of Eq. (16) with respect to all the elements of $\overline{\mathbf{n}}$ to obtain a Newton-type iterative minimization scheme. The Frechet-derivative of Eq. (16) is

$$\delta \mathbf{H}_s^{[M \times 1]} = \overline{\mathbf{G}}_{MC}^{[M \times 2L]} \cdot \left(\overline{\mathbf{n}}^{[2L \times L]} \cdot \delta \mathbf{H}_C^{[L \times 1]} + \overline{\mathbf{H}}_C^{[2L \times 2L]} \cdot \delta \mathbf{n}^{[2L \times 1]} \right). \quad (17)$$

We still need to derive the discretized total magnetic field $\mathbf{H}_C^{[L \times 1]}$ in the reconstruction domain with respect to $\mathbf{n}^{[2L \times 1]}$. From Eq. (11), we have

$$\delta \mathbf{H}_C^{[L \times 1]} = \delta \left[\left(\bar{\mathbf{I}}^{[L \times L]} - \bar{\mathbf{G}}_{CC}^{[L \times 2L]} \cdot \bar{\mathbf{n}}^{[2L \times L]} \right)^{-1} \right] \cdot \mathbf{H}_{C;i}^{[L \times 1]}. \quad (18)$$

It can further be shown that

$$\delta \bar{\mathbf{A}}^{-1} = -\bar{\mathbf{A}}^{-1} \cdot \delta \bar{\mathbf{A}} \cdot \bar{\mathbf{A}}^{-1} \quad (19)$$

holds as long as $\bar{\mathbf{A}}$ is regular. Using Eq. (19) in Eq. (18) with $\bar{\mathbf{A}} = (\bar{\mathbf{I}} - \bar{\mathbf{G}}_{CC} \cdot \bar{\mathbf{n}})$ and substituting the result into Eq. (17), yields

$$\delta \mathbf{H}_s^{[M \times 1]} = \bar{\mathbf{G}}_{MC}^{[M \times 2L]} \cdot \left[\bar{\mathbf{I}}^{[2L \times 2L]} + \bar{\mathbf{n}}^{[2L \times L]} \cdot \left(\bar{\mathbf{I}}^{[L \times L]} - \bar{\mathbf{G}}_{CC}^{[L \times 2L]} \cdot \bar{\mathbf{n}}^{[2L \times L]} \right)^{-1} \cdot \bar{\mathbf{G}}_{CC}^{[L \times 2L]} \right] \cdot \bar{\mathbf{H}}_C^{[2L \times 2L]} \cdot \delta \mathbf{n}^{[2L \times 1]}. \quad (20)$$

Each DBIM iteration consists of letting

$$\delta \mathbf{H}_s^{[M \times 1]} = \mathbf{H}_{Meas;s}^{[M \times 1]} - \mathbf{H}_{Calc;s}^{[M \times 1]}, \quad (21)$$

solving (20) for $\delta \mathbf{n}$, and computing the update

$$\mathbf{n}_{\nu+1}^{[2L \times 1]} = \mathbf{n}_{\nu}^{[2L \times 1]} + \delta \mathbf{n}_{\nu}^{[2L \times 1]}. \quad (22)$$

The new $\mathbf{n}_{\nu+1}$ is used to compute the $\mathbf{H}_{Calc;s}^{[M \times 1]}$ for the next iteration. ν is the iteration number of the current scatterer update.

Equation (20) can be simplified by using a Taylor series expansion of the matrix $(\bar{\mathbf{I}} - \bar{\mathbf{G}}_{CC} \cdot \bar{\mathbf{n}})^{-1}$:

$$\begin{aligned} \delta \mathbf{H}_s &= \bar{\mathbf{G}}_{MC} \cdot \left[\bar{\mathbf{I}} + \bar{\mathbf{n}} \cdot (\bar{\mathbf{I}} - \bar{\mathbf{G}}_{CC} \cdot \bar{\mathbf{n}})^{-1} \cdot \bar{\mathbf{G}}_{CC} \right] \cdot \bar{\mathbf{H}}_C \cdot \delta \mathbf{n} \\ &= \bar{\mathbf{G}}_{MC} \cdot (\bar{\mathbf{I}} - \bar{\mathbf{n}} \cdot \bar{\mathbf{G}}_{CC})^{-1} \cdot \delta \bar{\mathbf{n}} \cdot (\bar{\mathbf{I}} - \bar{\mathbf{G}}_{CC} \cdot \bar{\mathbf{n}})^{-1} \cdot \mathbf{H}_{C;i} \end{aligned} \quad (23)$$

with

$$\bar{\mathbf{G}}_{MC}^{[M \times 2L]} = \left[\bar{\mathbf{G}}_{MC}^x \mid \bar{\mathbf{G}}_{MC}^y \right]; \quad \bar{\mathbf{G}}_{CC}^{[L \times 2L]} = \left[\bar{\mathbf{G}}_{CC}^x \mid \bar{\mathbf{G}}_{CC}^y \right]; \quad \bar{\mathbf{H}}_C^{[2L \times 2L]} = \begin{bmatrix} \bar{\mathbf{H}} & \bar{\mathbf{0}} \\ \bar{\mathbf{0}} & \bar{\mathbf{H}} \end{bmatrix} \quad (24)$$

$$\bar{\mathbf{n}}^{[2L \times L]} = \begin{bmatrix} \bar{\mathbf{n}}_x \\ \text{---} \\ \bar{\mathbf{n}}_y \end{bmatrix}, \quad \delta \mathbf{n}^{[2L \times 1]} = \begin{bmatrix} \delta \mathbf{n}_x \\ \text{---} \\ \delta \mathbf{n}_y \end{bmatrix}, \quad \delta \bar{\mathbf{n}}^{[2L \times L]} = \begin{bmatrix} \delta \bar{\mathbf{n}}_x \\ \text{---} \\ \delta \bar{\mathbf{n}}_y \end{bmatrix}. \quad (25)$$

The submatrices $\bar{\mathbf{H}}$ in $\bar{\mathbf{H}}_C^{[2L \times 2L]}$ are diagonal and identical. Also the submatrices $\bar{\mathbf{n}}_x, \bar{\mathbf{n}}_y$ in $\bar{\mathbf{n}}^{[2L \times L]}$ and $\delta\bar{\mathbf{n}}_x, \delta\bar{\mathbf{n}}_y$ in $\delta\bar{\mathbf{n}}^{[2L \times L]}$ are diagonal matrices. The matrices which need to be inverted in Eq. (23) can now be written as

$$(\bar{\mathbf{I}} - \bar{\mathbf{G}}_{CC} \cdot \bar{\mathbf{n}}) = \left[\bar{\mathbf{I}} - (\bar{\mathbf{G}}_{CC}^x \cdot \bar{\mathbf{n}}_x + \bar{\mathbf{G}}_{CC}^y \cdot \bar{\mathbf{n}}_y) \right]^{[L \times L]}, \quad (26)$$

$$(\bar{\mathbf{I}} - \bar{\mathbf{n}} \cdot \bar{\mathbf{G}}_{CC}) = \left[\begin{array}{c|c} \bar{\mathbf{I}} - \bar{\mathbf{n}}_x \cdot \bar{\mathbf{G}}_{CC}^x & \bar{\mathbf{n}}_x \cdot \bar{\mathbf{G}}_{CC}^y \\ \hline \bar{\mathbf{n}}_y \cdot \bar{\mathbf{G}}_{CC}^x & \bar{\mathbf{I}} - \bar{\mathbf{n}}_y \cdot \bar{\mathbf{G}}_{CC}^y \end{array} \right]^{[2L \times 2L]}. \quad (27)$$

For the TM-polarization, we can derive a formula equivalent to Eq. (23) in the same way. It follows that:

$$\begin{aligned} \delta \mathbf{E}_s^\nabla &= \bar{\mathbf{G}}_{MC} \cdot \left[\bar{\mathbf{I}} + \bar{\mathbf{n}} \cdot (\bar{\mathbf{I}} - \bar{\mathbf{G}}_{CC} \cdot \bar{\mathbf{n}})^{-1} \cdot \bar{\mathbf{G}}_{CC} \right] \cdot \bar{\mathbf{E}}_C^\nabla \cdot \delta \mathbf{n} \\ &= \bar{\mathbf{G}}_{MC} \cdot (\bar{\mathbf{I}} - \bar{\mathbf{n}} \cdot \bar{\mathbf{G}}_{CC})^{-1} \cdot \delta \bar{\mathbf{n}} \cdot (\bar{\mathbf{I}} - \bar{\mathbf{G}}_{CC} \cdot \bar{\mathbf{n}})^{-1} \cdot \mathbf{E}_{C;i}^\nabla \end{aligned} \quad (28)$$

with

$$\bar{\mathbf{n}}^{[L \times 2L]} = [\bar{\mathbf{n}}_x \mid \bar{\mathbf{n}}_y]; \quad \delta \mathbf{n}^{[2L \times 1]} = \begin{bmatrix} \delta \mathbf{n}_x \\ - \\ \delta \mathbf{n}_y \end{bmatrix}; \quad \delta \bar{\mathbf{n}}^{[L \times 2L]} = [\delta \bar{\mathbf{n}}_x \mid \delta \bar{\mathbf{n}}_y]; \quad (29)$$

$$\delta \mathbf{E}_{C;i}^{\nabla;[2L \times 1]} = \begin{bmatrix} \delta \mathbf{E}_{i;x}^{\partial_x} \\ - \\ \delta \mathbf{E}_{i;y}^{\partial_y} \end{bmatrix}; \quad \delta \mathbf{E}_s^{\nabla;[2L \times 1]} = \begin{bmatrix} \delta \mathbf{E}_{s;x}^{\partial_x} \\ - \\ \delta \mathbf{E}_{s;y}^{\partial_x} \end{bmatrix}; \quad \bar{\mathbf{E}}_C^{\nabla;[L \times 2L]} = [\bar{\mathbf{E}}_x^{\partial_x} \mid \bar{\mathbf{E}}_y^{\partial_y}]; \quad (30)$$

$$\bar{\mathbf{G}}_{MC}^{[2M \times L]} = \begin{bmatrix} \bar{\mathbf{G}}_{MC}^x \\ - \\ \bar{\mathbf{G}}_{MC}^y \end{bmatrix}, \quad \bar{\mathbf{G}}_{CC}^{[2L \times L]} = \begin{bmatrix} \bar{\mathbf{G}}_{CC}^x \\ - \\ \bar{\mathbf{G}}_{CC}^y \end{bmatrix}. \quad (31)$$

where

$$(\bar{\mathbf{I}} - \bar{\mathbf{n}} \cdot \bar{\mathbf{G}}_{CC}) = \left[\bar{\mathbf{I}} - (\bar{\mathbf{G}}_{CC}^x \cdot \bar{\mathbf{n}}_x + \bar{\mathbf{G}}_{CC}^y \cdot \bar{\mathbf{n}}_y) \right]^{[L \times L]}, \quad (32)$$

$$(\bar{\mathbf{I}} - \bar{\mathbf{G}}_{CC} \cdot \bar{\mathbf{n}}) = \left[\begin{array}{c|c} \bar{\mathbf{I}} - \bar{\mathbf{n}}_x \cdot \bar{\mathbf{G}}_{CC}^x & \bar{\mathbf{n}}_y \cdot \bar{\mathbf{G}}_{CC}^x \\ \hline \bar{\mathbf{n}}_x \cdot \bar{\mathbf{G}}_{CC}^y & \bar{\mathbf{I}} - \bar{\mathbf{n}}_y \cdot \bar{\mathbf{G}}_{CC}^y \end{array} \right]^{[2L \times 2L]}. \quad (33)$$

To select elements for the scatterer contour from the elements of the previous iteration contained in the matrix $\bar{\mathbf{n}}$, we have to introduce a threshold above which all the selected elements are treated as elements of the scatterer. With this threshold, we can fill up a new vector $\mathbf{H}_C^{[L \times 1]}$ or $\mathbf{E}_{C;i}^{\nabla;[2L \times 1]}$ from

the computed magnetic or electric field of the previous iteration, respectively. With this procedure, the size of the investigated reconstruction problem shrinks with the subsequent iterations.

We used a conjugate gradient (CG) scheme to invert the matrix equation (11) for the forward problem as well as Eq. (20) for the inverse problem. For solving Eq. (11) the product $\overline{\mathbf{G}}_{CC} \cdot \mathbf{J}_s$ needs to be computed i times where i is the number of CG iterations and $\mathbf{J}_s = \overline{\mathbf{n}} \cdot \mathbf{H}_C$. The same situation applies to Eq. (20) for which the occurring vector matrix products are successively solved from the right to the left for each CG iteration, too. Instead of computing the matrix-vector product directly, which has a computational complexity of $\mathcal{O}(L^2)$, the Multilevel Fast Multipole Algorithm (MLFMA) is used which has a computational complexity of $\mathcal{O}(L \log(L))$.

III. FUNDAMENTALS OF THE MULTILEVEL FAST MULTIPOLE ALGORITHM

In MLFMA, the interactions of source and observation points, which are represented by the Green's matrices $\overline{\mathbf{G}}_{CC}$ and $\overline{\mathbf{G}}_{MC}$, are divided by aggregation of source points and disaggregation of observation points to source point groups and observation point groups, respectively. Only the source point and observation point group representatives interact with each other. Each source and each observation point only interacts with its related source point group and observation point group representative. With this principle, the number of total interactions can be reduced from $N \times M$ source-observation-point interactions, where N is the number of source and M the number of observation points, to $N + \frac{N}{L_s} \cdot \frac{M}{L_{ob}} + M$ number of interactions with L_s and L_{ob} denoting the number of source and observation point groups, respectively. Figure 1 illustrates the reduction of interactions by aggregating source and disaggregating observation points to groups. To aggregate source and disaggregate observation points we have to introduce the aggregated source-point and disaggregated observation-point locations in the argument of the Hankel function which represents the elements of the Green's matrices $\overline{\mathbf{G}}_{CC}$ and $\overline{\mathbf{G}}_{MC}$. With

$$H_\nu^{(1)}(k|\mathbf{R}_j - \mathbf{R}_i|) e^{j\nu\varphi_{ji}} = H_\nu^{(1)}(kr_{ji}) e^{j\nu\varphi_{ji}} \quad (34)$$

we can define aggregated source-point and disaggregated observation-point locations grouping source and observation points according to

$$\mathbf{r}_{ji} = \underbrace{\mathbf{R}_j - \mathbf{R}_{j'}}_{=\mathbf{r}_{j'}} + \underbrace{\mathbf{R}_{j'} - \mathbf{R}_l}_{=\mathbf{r}_{j'l}} + \underbrace{\mathbf{R}_l - \mathbf{R}_i}_{=\mathbf{r}_{li}} \quad (35)$$

where \mathbf{R}_i and \mathbf{R}_j are the source-point and the observation-point locations, respectively. \mathbf{R}_l and $\mathbf{R}_{j'}$ are the aggregated source-point and the disaggregated observation-point locations.

After a two-stage application of the Hankel function addition theorem with $|\mathbf{r}_{li}| < |\mathbf{r}_{l'l}|$ and $|\mathbf{r}_{j'l'}| < |\mathbf{r}_{l'i}|$, Eq. (34) can be written as

$$H_\nu^{(1)}(kr_{ji}) e^{j\nu\varphi_{ji}} = e^{j\nu(\varphi_{l'i} + \pi)} \sum_m J_m(kr_{j'l'}) e^{jm(\varphi_{j'l'} - \pi)} \sum_n H_{m-n-\nu}^{(1)}(kr_{l'l}) e^{-j(m-n)\varphi_{l'l}} J_n(kr_{li}) e^{-jn\varphi_{li}}. \quad (36)$$

Now, we can introduce the integral representation of the Bessel functions according to

$$J_m(kr_{j'l'}) e^{\pm jm\varphi_{j'l'}} = \frac{1}{2\pi} \int_{-\pi}^{\pi} e^{jkr_{j'l'} \cos(\vartheta \mp \varphi_{j'l'})} e^{jm(\vartheta - \pi/2)} d\vartheta \quad (37)$$

and exchange the order of the integrals with the series expansion. After using the sifting property of the δ -distribution, we obtain

$$H_\nu^{(1)}(kr_{ji}) e^{j\nu\varphi_{ji}} = \frac{e^{j\nu\pi}}{2\pi} \int_{-\pi}^{\pi} \beta_{j'l'}(\vartheta) \alpha_{l'l}(\vartheta) \beta_{li}(\vartheta) d\vartheta \quad (38)$$

where

$$\beta_{j'l'}(\vartheta) = e^{jkr_{j'l'} \cos(\vartheta - \varphi_{j'l'})}; \quad \alpha_{l'l}(\vartheta) = \sum_p j^p e^{j\vartheta p} H_{p-\nu}^{(1)}(kr_{l'l}) e^{-j(p-\nu)\varphi_{l'l}}; \quad \beta_{li}(\vartheta) = e^{jkr_{li} \cos(\vartheta - \varphi_{li})}. \quad (39)$$

The integration over ϑ can be expressed by a Q -point summation

$$H_\nu^{(1)}(kr_{ji}) e^{j\nu\varphi_{ji}} = \frac{e^{j\nu\pi}}{Q} \sum_{q=1}^Q \beta_{j'l'}(\vartheta_q) \alpha_{l'l}(\vartheta_q) \beta_{li}(\vartheta_q) \quad (40)$$

with the aggregation operator $\underline{\beta}_{j'l'}$, the disaggregation operator $\underline{\beta}_{li}$ and the diagonalized translation operator $\bar{\alpha}_{l'l}$ in accordance with:

$$\underline{\beta}_{j'l'} = \begin{pmatrix} \beta_{j'l'}(\vartheta_1) \\ \vdots \\ \beta_{j'l'}(\vartheta_Q) \end{pmatrix}; \quad \underline{\beta}_{li} = \begin{pmatrix} \beta_{li}(\vartheta_1) \\ \vdots \\ \beta_{li}(\vartheta_Q) \end{pmatrix}; \quad \bar{\alpha}_{l'l} = \begin{pmatrix} \alpha_{l'l}(\vartheta_1) & \dots & 0 \\ \vdots & \ddots & \vdots \\ 0 & \dots & \alpha_{l'l}(\vartheta_Q) \end{pmatrix}. \quad (41)$$

Now, we are able to nest this algorithm into itself by the aggregation of the source point groups and the disaggregation of the observation point groups to bigger source and observation point groups, respectively. For $\mathcal{O}(N)$ number of source and observation points, this Fast Multipole Algorithm can be nested into itself $\log(N)$ times with inter- and ant interpolation which leads to the tree structure of the MLFMA in Figure 2. Basically, in the MLFMA, cylindrical waves are replaced by an integration (summation) of plane waves which lead to the diagonalization of the translation operator α . Each

level has a computational complexity of $\mathcal{O}(N)$. Thus, with $\log(N)$ -levels the total cost is $\mathcal{O}(N \log N)$ [7], [8]. Apart from the lower computational complexity, the storage requirement using MLFMA is also only $\mathcal{O}(N \log N)$ compared to direct computation requiring $\mathcal{O}(N^2)$ memory.

Figure 3 represents the multilevel tree structure of Figure 2 in two dimensions for three levels. In the upper left figure each dot represents a group center. The smallest rectangles are groups of the lowest level with their pertinent group centers. Those source groups on the lowest level without a group center are considered to be empty. All others (i.e. the left and upper strip of the upper left figure, which are source point groups) contain one or more subscatterers. Four source groups are aggregated to one larger source group on the next higher level. On this higher level, four of these larger source groups in turn are aggregated to the next larger one on the next upper level from where they are translated to the observation point groups. Only one observation point group is displayed in the upper left figure which is surrounded by not considered source point groups. These source point groups are not necessarily empty but cannot be treated on the uppermost level since they are direct neighbors to the observation point group. Source and observation point groups of the same level must not overlap¹ This results from the derivation of Eq. (34) after a two-stage application of the Hankel function addition theorem under the condition that $|\mathbf{r}_{li}| < |\mathbf{r}_{l'l}|$ and $|\mathbf{r}_{j'l'}| < |\mathbf{r}_{l'i}|$ is satisfied. If source and observation point groups of the same level overlapped each other, both these conditions would not be satisfied and the Hankel function addition theorem would not be valid for the overlapping regions. Thus, overlapping source and observation point groups would lead to oscillatory and unstable results. Practice has shown that it is reasonable to leave a space of one group size between translated source point groups and observation point groups to avoid numerical instabilities. Therefore, we have to treat the source point groups not considered on the uppermost level, on the next lower level, as depicted in the upper right figure of Figure 3. Here, we can see that the algorithm scheme is basically the same as one at one level above. On the next lower level (the first level) no aggregation of source point groups are possible anymore. The source point groups are directly translated to the observation point groups. The lower left figure of Figure 3 shows only one observation point group to which the source point groups are translated. The lower right figure of Figure 3 shows the near neighbor interaction with the observation point in the center of the observation point group. These interactions have to be treated directly. Finally, the translated results to the center of the upper most observation point group shown in the upper left figure of

¹Of course, in the global MLFMA scheme source and observation points are allowed to overlap and do overlap.

Figure 3 can be disaggregated to the next finer observation point group via the disaggregation operator $\beta_{j\nu}$. This result can now be superimposed with the result obtained at one level below from the translated source point groups to the observation point group in the center of the upper right figure of Figure 3. In the next step the superimposed result can be disaggregated to the next lower level where it is added to the result obtained by the source point center translations on the first level. If the observation point is in the center of the observation point group, no disaggregation operation is necessary anymore and the total result of all three levels can be added to the direct interaction result shown in the lower right figure of Figure 3.

IV. HALF-QUADRATIC REGULARIZATION

Usually, the number of measurement points M on the measurement surface is less than the number of cells N in the reconstruction domain, resulting in an under-determined matrix equation (23). Just increasing the number of observation points on the measurement surface, so that M becomes equal to N , does not solve the problem, since the added measurement data resemble each other due to a denser sampling on the measurement surface, which leads to a very ill-conditioned matrix equation. But since the matrix equation (23) also depends on the frequency ω and the angle of the incident field, we can consider frequency and/or angular diversity to build a matrix equation system with more diverse data. Additionally, a regularization scheme needs to be introduced to overcome the still ill-conditioned matrix equation system. We choose the half-quadratic regularization principle which has the property of preserving edges while smoothing homogeneous domains of the object function [9], [10].

From Eq. (23), we can build a matrix equation system which includes all the different frequency and/or angular diversity experiments. The normal equation of such an unconstrained minimization problem can be written in a form appropriate for specifying the half-quadratic regularization scheme:

$$\left(\overline{\mathbf{A}}^T \cdot \overline{\mathbf{A}} + \lambda \overline{\mathbf{D}}^T \cdot \overline{\mathbf{B}}^T \cdot \overline{\mathbf{B}} \cdot \overline{\mathbf{D}}\right) \cdot \delta \mathbf{n} = \overline{\mathbf{A}}^T \cdot \mathbf{d} \quad (42)$$

where $\delta \mathbf{n}$ is the object function update. The object function for perfectly electric conducting scatterers is a real quantity. The \mathbf{d} -vector contains the differences between the computed scattered field from the last reconstruction update and the measured scattered field in accordance with Eq. (21) for all the different frequency and/or angular diversity experiments. The matrix $\overline{\mathbf{B}}$ in Eq. (42)

consists of eight diagonal submatrices, according to

$$\overline{\mathbf{B}} = [\text{diag}\{\sqrt{(b_x^x)_l}\}, \text{diag}\{\sqrt{(b_x^y)_l}\}, \text{diag}\{\sqrt{(b_y^x)_l}\}, \dots, \text{diag}\{\sqrt{(b_{d1}^y)_l}\}, \text{diag}\{\sqrt{(b_{d2}^x)_l}\}, \text{diag}\{\sqrt{(b_{d2}^y)_l}\}]^T. \quad (43)$$

These diagonal submatrices contain the regularization weights for the numerically computed gradients corresponding to the differences of the elements in the x , y , and both diagonal-directions. Since $\delta \mathbf{n}$ contains the update of the normal elements of both Cartesian directions, the total number of submatrices contained in $\overline{\mathbf{B}}$ is eight. $\overline{\mathbf{D}}$ is the matrix which also consists of eight submatrices to perform the gradient computation for the pertinent directions, according to

$$\overline{\mathbf{D}} = [\{\overline{\mathbf{D}}_x^x\}^T, \{\overline{\mathbf{D}}_x^y\}^T, \{\overline{\mathbf{D}}_y^x\}^T, \{\overline{\mathbf{D}}_y^y\}^T, \{\overline{\mathbf{D}}_{d1}^x\}^T, \{\overline{\mathbf{D}}_{d1}^y\}^T, \{\overline{\mathbf{D}}_{d2}^x\}^T, \{\overline{\mathbf{D}}_{d2}^y\}^T]^T \quad (44)$$

where for instance the submatrices $\overline{\mathbf{D}}_x^x$ for the x -direction and $\overline{\mathbf{D}}_y^y$ for the y -direction are given by

$$\overline{\mathbf{D}}_x^x = \overline{\mathbf{D}}_x^y = \frac{1}{\delta} \begin{pmatrix} 1 & -1 & 0 & \dots & 0 & 0 \\ 0 & 1 & -1 & \dots & 0 & 0 \\ \vdots & & & \ddots & & \vdots \\ 0 & 0 & 0 & \dots & 1 & -1 \end{pmatrix}. \quad (45)$$

δ in Eq. (45) is the scaling parameter which determines the value above which a gradient is emphasized and below which it is smoothed. According to the principles of half-quadratic regularization [9], the weighting coefficients $(b)_k$ in Eq. (43) are given by the expression $(b^{\nu+1})_k = \phi'(Df)/2(Df)$ where the potential function $\phi(t)$ was chosen to be $\phi(t) = t^2/(1+t^2)$. With $\phi'(t)/(2t) = 1/((1+t^2)^2)$, one can see that for $t \rightarrow \infty$, $b = 0$, and for $t \rightarrow 0$, $b = 1$. So larger gradient components, expressed by t , yield a lower local regularization penalty. The strategy to compute the regularization weights can be summarized as follows: First, the regularization weights are computed from the last scatterer update with the proposed potential function $\phi(t)$. These regularization weights $(b^{\nu+1})_k$ are used and kept constant for the computation of the next scatterer update via DBIM. From this new scatterer update the next set of regularization weights is computed and the DBIM iteration is repeated.

In addition, as mentioned before, through the regularization described above, smoothed domains are clipped off to reduce the computational burden further. After these domains are clipped, they are not considered in the subsequent iteration process any longer. λ in Eq. (42) is the global regularization parameter with which the condition number of the matrix in Eq. (42) can be adjusted.

A. Iteration Scheme

Now we summarize the steps necessary to compute the next scatterer update: First, we start with the initial guess that the scatterer is equivalent to the background so that the total field is approximated by the incident field. After the first scatterer reconstruction, the total field in the reconstruction domain is computed as many times as the number of different incident field directions and frequencies. From this result and the previous scatterer reconstruction, the scattered field on the measurement surface can be computed. The error between the measured and the scattered field can be determined by

$$F^{\nu+1} = \frac{\| \text{Measured field data} - \text{Computed field data} \|}{\| \text{Measured field data} \|}, \quad (46)$$

where ν is the current iteration stage in the DBIM process. The location-dependent regularization weights $(b^{\nu+1})_k$ are computed as explained in Section IV. The next scatterer update can now be computed from the new regularization parameter weights and the total field which was computed from the last scatterer update. The whole iteration process is depicted in Figure 4.

V. RECONSTRUCTION CONFIGURATION AND NUMERICAL RESULTS

Figures 5 to 7 show the reconstruction results for metallic two-dimensional scatterers using the algorithm of Section IV. The reconstruction domain was chosen to be 3.0×3.0 meters. A single- or multi-frequency incident field excitation was chosen around the scatterer domain with a polarization orthogonal to the cylinder axis of the scatterer cross-section (TE-case). The object was illuminated from all directions with the incident fields in equidistant angles around the reconstruction domain and enclosed by a circular measurement surface where the synthetically generated data were sampled in equispaced angles. The final frame of Figures 5 to 7 show the true scatterer shape and the other frames show successive DBIM iterations. The gray levels correspond to the norm of the estimated \mathbf{n} . Each pixel also has a direction, which is not being shown. In Figure 5 the reconstruction of a ‘single kite’ is shown for which the discretization in the reconstruction domain was chosen to be 90×90 pixels. We can see that there is hardly any change in the scatterer update visible from the 5th to the 7th iteration. The reconstruction result remains stable.

Figure 6 shows the reconstruction of a ‘double kite’. In this case the discretization was chosen to be 50×50 samples. There is hardly any further progress from iteration 8 to 15, though there are still distortions in one of the ‘kites’. The reason is that the described minimization scheme found a local minimum in the neighborhood of the global minimum.

Figure 7 shows the reconstruction of the cross-section of an airplane model. In contrast to both of the previous reconstruction examples, a multi-frequency excitation was used with four frequencies from $k_{min} = 1.5$ to $k_{max} = 9.2$. The final reconstruction result is shown in iteration 15.

VI. CONCLUSIONS

We implemented a Multilevel Fast Multipole Algorithm specially adapted to the Distorted Born Iterative Method. The MLFMA was used to solve the forward problem as well as all the Green's matrix-vector products of the inversion branch of the DBIM for each iteration update. Because of the inherent ill-posedness of the inverse problem the principle of half-quadratic regularization was introduced. The reconstruction results presented show a very good agreement with the original shapes of the scatterers for the different examples. The computational complexity as well as the storage requirements are considerably less than without using the MLFMA.

APPENDIX

A. Derivation of the integral equations

Starting with the decoupling of Maxwell's equations for a homogeneous, isotropic medium with constant permeability μ_0 and permittivity ϵ_0 , we obtain, for the total magnetic field $\mathbf{H}(\mathbf{R}, \omega)$

$$\nabla \times [\tilde{\epsilon}^{-1}(\mathbf{R}) \nabla \times \mathbf{H}(\mathbf{R}, \omega)] - \omega^2 \mu_0 \mathbf{H}(\mathbf{R}, \omega) = \nabla \times [\tilde{\epsilon}^{-1}(\mathbf{R}) \mathbf{J}_q(\mathbf{R}, \omega)] \quad (47)$$

with

$$\tilde{\epsilon}(\mathbf{R}) = \frac{j\omega\epsilon(\mathbf{R}) - \sigma(\mathbf{R})}{j\omega}, \quad (48)$$

where \mathbf{J}_q on the right-hand side of Eq. (47) represents the primary sources, and μ , ϵ and σ in Eq. (48) are the permeability, the permittivity and the conductivity of the scatterer, respectively. The electromagnetic scattering problem can be reduced to a scalar two-dimensional scattering problem for two different polarization cases if the scatterer is quasi two-dimensional (i.e. if the scatterer is a cylinder with infinitely long axis). We can distinguish the Transverse Magnetic (TM) case, for which the polarization vector $\hat{\mathbf{E}}_0$ of the incident field is in alignment with the cylinder axis of the scatterer, and the Transverse Electric (TE) case, for which the polarization vector is in a plane perpendicular to the scatterer's cylinder axis. In the latter case, the magnetic field $\mathbf{H}(\mathbf{R}, \omega)$ has only one component in the direction of the cylinder axis; thus, $\mathbf{H}(\mathbf{R}, \omega) = H_z \mathbf{e}_z$ and $H_z(x, y, z = \text{const})$.

Additionally, for $\mu_0 \nabla \cdot \mathbf{H}(\mathbf{R}, \omega) = 0$, it follows from (47) that

$$\nabla \cdot [\tilde{\epsilon}^{-1}(\mathbf{R}) \nabla H_z(\mathbf{R}, \omega)] + \omega^2 \mu_0 H_z(\mathbf{R}, \omega) = -\nabla \times [\tilde{\epsilon}^{-1}(\mathbf{R}) \mathbf{J}_q(\mathbf{R}, \omega)] . \quad (49)$$

Inserting $\nabla \cdot (\epsilon_0^{-1} \nabla H_z)$ in Eq. (49) we can define the secondary equivalent sources $\mathbf{J}_c(\mathbf{R}, \omega)$ in Eq. (51). With the wavenumber k for the lossless background medium $k^2 = \omega^2 \mu_0 \epsilon_0$, we have

$$(\Delta + k^2) H_z(\mathbf{R}, \omega) = -\nabla \times [\mathbf{J}_q(\mathbf{R}, \omega) + \mathbf{J}_c(\mathbf{R}, \omega)] \cdot \mathbf{e}_z \quad (50)$$

$$= -\nabla \times \mathbf{J}_q(\mathbf{R}, \omega) \cdot \mathbf{e}_z + \nabla \cdot \left[\underbrace{\left(1 - \frac{\epsilon_0}{\tilde{\epsilon}(\mathbf{R})} \right)}_{= O(\mathbf{R})} \nabla H_z(\mathbf{R}, \omega) \right] . \quad (51)$$

The object function $O(\mathbf{R})$ is defined by the electromagnetic material parameters ϵ_0 and $\tilde{\epsilon}(\mathbf{R})$ according to Eq. (51).

Since the electromagnetic scattering problem is reduced to an equivalent scalar one, we only need to consider the free space two-dimensional scalar Green's function:

$$G(\mathbf{R}, \mathbf{R}', \omega) = \frac{j}{4} H_0^{(1)}(k|\mathbf{R} - \mathbf{R}'|) . \quad (52)$$

Applying Green's theorem to Eq. (50) yields

$$H_z(\mathbf{R}, \omega) = H_z^i(\mathbf{R}, \omega) + \underbrace{\mathbf{e}_z \cdot \int_{S_M} [\nabla' \times \mathbf{J}_c(\mathbf{R}', \omega)] G(\mathbf{R}, \mathbf{R}', \omega) d^2 R'}_{= H_z^s(\mathbf{R}, \omega)} . \quad (53)$$

$H_z(\mathbf{R}, \omega)$, $H_z^i(\mathbf{R}, \omega)$ and $H_z^s(\mathbf{R}, \omega)$ in Eq. (53) are z -components of the total, incident and scattered magnetic fields, respectively, and S_M denotes the 2D-reconstruction domain which includes all the scatterers.

Integrating Eq. (53) by parts leads to a further simplification of the magnetic scattered field:

$$\begin{aligned} H_z^s(\mathbf{R}, \omega) &= \mathbf{e}_z \cdot \int_{S_M} \nabla' \times [\mathbf{J}_c(\mathbf{R}', \omega) G(\mathbf{R}, \mathbf{R}', \omega)] d^2 R' - \mathbf{e}_z \cdot \int_{S_M} \nabla' G(\mathbf{R}, \mathbf{R}', \omega) \times \mathbf{J}_c(\mathbf{R}', \omega) d^2 R' \\ &= -\mathbf{e}_z \cdot \int_{S_M} \nabla' G(\mathbf{R}, \mathbf{R}', \omega) \times \mathbf{J}_c(\mathbf{R}', \omega) d^2 R' + \underbrace{\mathbf{e}_z \cdot \int_{C_M} \mathbf{n}' \times [\mathbf{J}_c(\mathbf{R}', \omega) G(\mathbf{R}, \mathbf{R}', \omega)] dR'}_{= 0} . \end{aligned} \quad (54)$$

The last integral of Eq. (54) is equal to zero since $\mathbf{J}_c(\mathbf{R}', \omega)$ is equal to zero on the contour C_M which describes the boundary of the reconstruction domain S_M . In the following, we want to substitute

the equivalent secondary sources according to Eq. (51) in Eq. (53), for which it follows:

$$H_z(\mathbf{R}, \omega) = H_z^i(\mathbf{R}, \omega) - \underbrace{\int_{S_M} \int \nabla' \cdot \left\{ \left[1 - \frac{\epsilon_0}{\tilde{\epsilon}(\mathbf{R}')} \right] \nabla' H_z(\mathbf{R}', \omega) \right\} G(\mathbf{R}, \mathbf{R}', \omega) d^2 R'}_{= H_z^s(\mathbf{R}, \omega)} . \quad (55)$$

By the same method used to obtain Eq. (54), it follows after performing the partial integration on Eq. (55)

$$H_z(\mathbf{R}, \omega) = H_z^i(\mathbf{R}, \omega) + \int_{S_M} O(\mathbf{R}') \nabla' H_z(\mathbf{R}', \omega) \cdot \nabla' G(\mathbf{R}, \mathbf{R}', \omega) d^2 R' . \quad (56)$$

A.1 Definitions and properties of the equivalent secondary sources

We define the object function according to Eq. (51) as

$$O(\mathbf{R}) = 1 - \frac{j\omega\epsilon_0}{j\omega\epsilon(\mathbf{R}) - \sigma(\mathbf{R})} . \quad (57)$$

Outside the scatterer volume S_q the conductivity $\sigma = 0$ and the permittivity ϵ is equal to the background permittivity ϵ_0 . For the inner domain of the scatterer volume S_q , we suppose that $\omega\epsilon \ll \sigma$ and $\omega\epsilon_0 \ll \sigma$, which holds for all practical applications on metallic scatterers. With these assumptions, the object function becomes

$$O(\mathbf{R}) \begin{cases} \simeq 1 & \text{for } \mathbf{R} \in S_c \\ 0 & \text{else } \mathbf{R} \notin S_c . \end{cases} \quad (58)$$

In the case of a perfect electric conductor with $\sigma \rightarrow \infty$, the object function $O(\mathbf{R})$ becomes a two-dimensional unit-step function, according to

$$\Gamma(\mathbf{R}) = \begin{cases} 1 & \text{for } \mathbf{R} \in S_c \\ 0 & \text{else } \mathbf{R} \notin S_c \end{cases} \quad (59)$$

which is equal to unity for \mathbf{R} inside the two-dimensional scatterer domain S_c and zero outside. One can define this unit-step function by a potential function $\Phi(\mathbf{R})$ so that

$$\Gamma(\mathbf{R}) = u(\Phi(\mathbf{R})) \quad \text{with} \quad \Phi(\mathbf{R}) \begin{cases} < 0 & \text{for } \mathbf{R} \notin V_c \cup S_c \\ = 0 & \text{for } \mathbf{R} \in S_c \\ > 0 & \text{for } \mathbf{R} \in V_c \setminus S_c . \end{cases} \quad (60)$$

Performing the derivative of this two-dimensional unit-step function as shown in Eq. (61), we can define a two-dimensional² vector singular function according to

$$\boldsymbol{\gamma}(\mathbf{R}) = -\nabla\Gamma(\mathbf{R}) = \delta(\Phi(\mathbf{R})) \nabla\Phi(\mathbf{R}) = \delta(\Phi(\mathbf{R})) |\nabla\Phi(\mathbf{R})| \mathbf{n} = \gamma(\mathbf{R}) \mathbf{n} \quad (61)$$

with outward unit normal of the scatterer $\mathbf{n} = \nabla\Phi(\mathbf{R})/|\nabla\Phi(\mathbf{R})|$. With this definition we are able to find an expression equivalent for the right-hand side of Eq. (51) for the secondary equivalent current sources:

$$\mathbf{J}_c(\mathbf{R}, \omega) = \gamma(\mathbf{R}) \mathbf{J}_s(\mathbf{R}, \omega) = -\mathbf{n}(\mathbf{R}) \cdot \nabla\Gamma(\mathbf{R}) \mathbf{J}_s(\mathbf{R}, \omega) . \quad (62)$$

This secondary equivalent current density $\mathbf{J}_c(\mathbf{R}, \omega)$ is singular on the contour of the scatterer and is equal to zero everywhere else according to the definitions in Eq. (61). $\mathbf{J}_s(\mathbf{R}, \omega)$ is the surface current density of secondary equivalent sources and S_c is the scatterer domain enclosed by the contour C of the scatterer. Substituting the result of Eq. (62) in Eq. (54) yields

$$H_z^s(\mathbf{R}, \omega) = \int \int_{S_M} \nabla'\Gamma(\mathbf{R}') \cdot \mathbf{n}' [\mathbf{e}_z \cdot \nabla'G(\mathbf{R}, \mathbf{R}', \omega) \times \mathbf{J}_s(\mathbf{R}', \omega)] d^2R' . \quad (63)$$

Performing an integration by parts and making use of Gauss' theorem, we find the scattered magnetic field

$$\begin{aligned} H_z^s(\mathbf{R}, \omega) &= - \int \int_{S_c} \nabla' \cdot [\mathbf{n}' \mathbf{e}_z \cdot \nabla'G(\mathbf{R}, \mathbf{R}', \omega) \times \mathbf{J}_s(\mathbf{R}', \omega)] d^2R' \\ &= - \int_C \underbrace{\mathbf{n}' \cdot \mathbf{n}'}_{=1} [\mathbf{e}_z \cdot \nabla'G(\mathbf{R}, \mathbf{R}', \omega) \times \mathbf{J}_s(\mathbf{R}', \omega)] dR' \end{aligned} \quad (64)$$

with C as the contour of the scatterer. For perfectly conducting scatterers the boundary conditions

$$\left. \begin{aligned} \mathbf{n} \times \mathbf{E}(\mathbf{R}, \omega) &= 0 \\ \mathbf{n} \times \mathbf{H}(\mathbf{R}, \omega) &= \mathbf{J}_s(\mathbf{R}, \omega) \end{aligned} \right\}, \quad \text{for } \mathbf{R} \in C \text{ and } \sigma \longrightarrow \infty \quad (65)$$

must be satisfied. Inserting this boundary condition in Eq. (64), it follows that the magnetic scattered field is

$$\begin{aligned} H_z^s(\mathbf{R}, \omega) &= -\mathbf{e}_z \cdot \int_C \nabla'G(\mathbf{R}, \mathbf{R}', \omega) \times [\mathbf{n}' \times H_z(\mathbf{R}', \omega) \mathbf{e}_z] dR' = \int_C \mathbf{n}' \cdot \nabla'G(\mathbf{R}, \mathbf{R}', \omega) H_z(\mathbf{R}', \omega) dR' \\ &= \frac{j}{4} \int_C \mathbf{n}' \cdot \nabla' H_0^{(1)}(k|\mathbf{R} - \mathbf{R}'|) J_s(\mathbf{R}', \omega) dR' \end{aligned} \quad (66)$$

²This is not only limited to two dimensions but can also be used for three or n dimensions.


with $H_z(\mathbf{R}, \omega) \mathbf{e}_z = J_s(\mathbf{R}, \omega)[\mathbf{e}_t \times \mathbf{n}(\mathbf{R})]$ for $\mathbf{R} \in C$. \mathbf{e}_t is a tangential vector along the scatterer contour C .

We obtain a boundary integral equation, which can be solved in discretized form for the total magnetic field from the knowledge of the normal vector $\mathbf{n} = \mathbf{n}(\mathbf{R})$:


$$H_z^i(\mathbf{R}, \omega) = \int_{\mathbf{R}' \in C} H_z(\mathbf{R}', \omega) (\delta(\mathbf{R} - \mathbf{R}') - \mathbf{n}(\mathbf{R}') \cdot \nabla' G(\mathbf{R}, \mathbf{R}', \omega)) dR' . \quad (67)$$

REFERENCES

- [1] Roger, A., "Newton-Kantorovitch algorithm applied to an electromagnetic inverse problem", IEEE Trans. Ant. Prop., Vol. 29, 232-238, 1981.
- [2] Bonnard, S., P. Vincent and M. Saillard, "Cross-borehole inverse scattering using a boundary finite-element method", Inverse Problems, Vol. 14, 521-534, 1998.
- [3] Chiu, C.-C. and Y.-W. Kiang, "Microwave imaging of multiple conducting cylinders", IEEE Trans. Ant. Prop., Vol. 40, 933-941, 1992.
- [4] Chiu, C.-C. and Y.-W. Kiang, "Electromagnetic imaging for an imperfectly conducting cylinder", IEEE Trans. Ant. Prop., Vol. 39, 1632-1639, 1991.
- [5] Chew, W.C. and Y.M. Wang, "Reconstruction of two-dimensional permittivity distribution using the distorted Born iterative method", IEEE Trans. Med. Imaging, Vol. 9, 218-225, 1990.
- [6] Joachimowicz, N., C. Pichot and J.P. Hugonin, "Inverse scattering: an iterative numerical method for electromagnetic imaging", IEEE Trans. Ant. Prop., Vol. 39, 1742-1751, 1991.
- [7] Lu, C.-C. and W.C. Chew, "A multilevel algorithm for solving a boundary integral equation of wave scattering", Microwave Opt. Technol. Lett., Vol. 7, 466-470, 1994.
- [8] Song, J.M. and W.C. Chew, "Multilevel Fast-Multipole Algorithm for solving combined field integral equations of electromagnetic scattering", Microwave Opt. Technol. Lett., Vol. 10, 14-19, 1995.
- [9] Charbonnier, P., L. Blanc-Féraud, G. Aubert, and M. Barlaud, "Deterministic edge-preserving regularization in computed imaging", IEEE Trans. Image Processing, Vol. 6, 298-311, 1997.
- [10] Lobel, P., L. Blanc-Féraud, C. Pichot and M. Barlaud, "A new regularization scheme for inverse scattering", Inverse Problems, Vol. 13, 403-410, 1997.
- [11] Brandfaß, M. and W.C. Chew, "Microwave imaging as applied to remote sensing making use of a multilevel fast multipole algorithm", Proc. SPIE's International Symposium on Aerospace/Defense Sensing and Controls – Aerosense 2000, Orlando/FL, USA, 2000.



Michael Brandfass received the B.S., M.S., and Ph.D. degrees in electrical engineering from the University of Kassel, Germany in 1988, 1990 and 1996, respectively. From 1990 to 1996 he was with the Dept. of Elec. Eng. at the University of Kassel as a Research Scientist. From 1996 to 1997 he was with the German Aerospace Research Establishment (DLR), Oberpfaffenhoffen, Germany before he joined the Center of Computational Electromagnetics at the University of Illinois, Urbana-Champaign as a Postdoctoral Research Associate in 1997. His research interests have been in inverse scattering, SAR-processing, and fast algorithms based on multipole methods and wavelets.



Weng Cho Chew received the B.S. degree in 1976, both the M.S. and Engineer's degrees in 1978, and the Ph.D. degree in 1980, all in electrical engineering from the Massachusetts Institute of technology, Cambridge. From 1981 to 1985, he was with Schlumberger-Doll Research, Ridgefield, CT, as a Program Leader and later as a Department Manager. From 1985 to 1990, he was an Associate Professor with the University of Urbana-Champaign. Presently, he is a Professor and the Director of the Center for Computational Electromagnetics at the same university. He was an NSF Presidential Young Investigator for 1986. He has been active with various journals and societies. He published more than 400 scientific

journal and conference papers and is the author of the book *Waves and Fields in Inhomogeneous Media*.

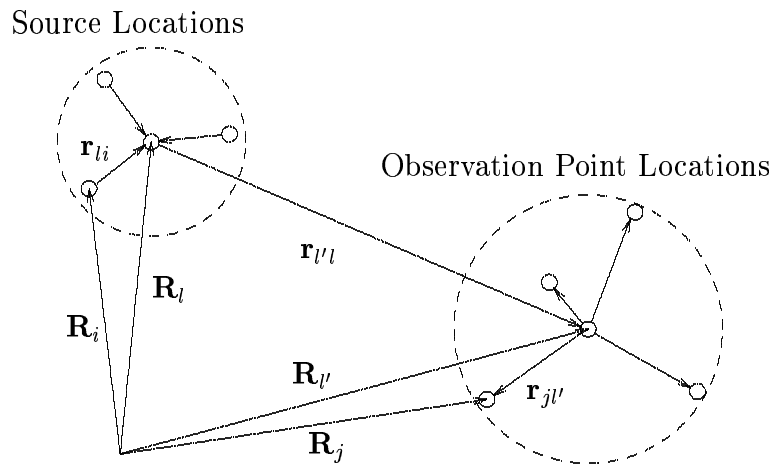


Fig. 1.

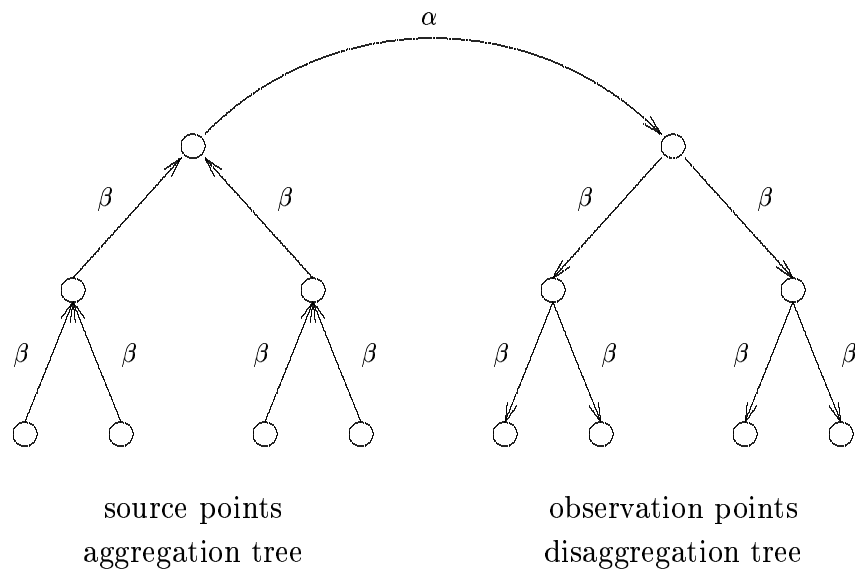


Fig. 2.

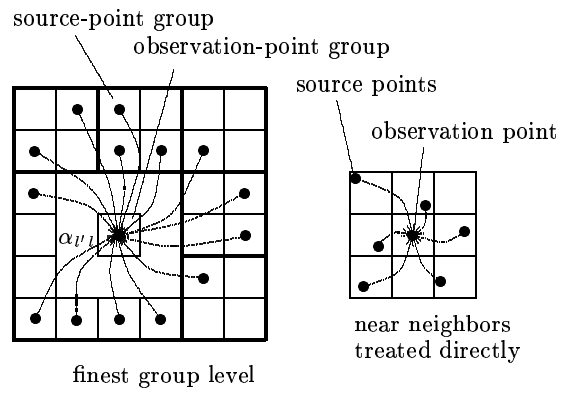
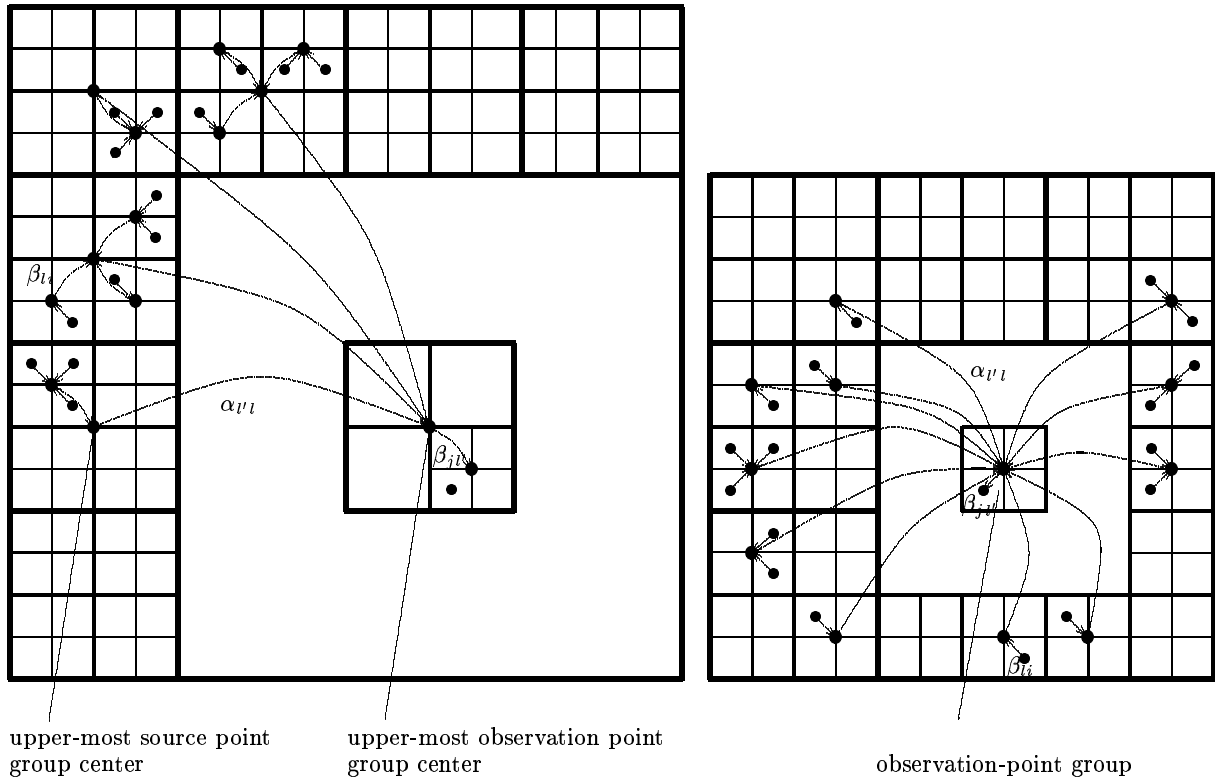


Fig. 3.

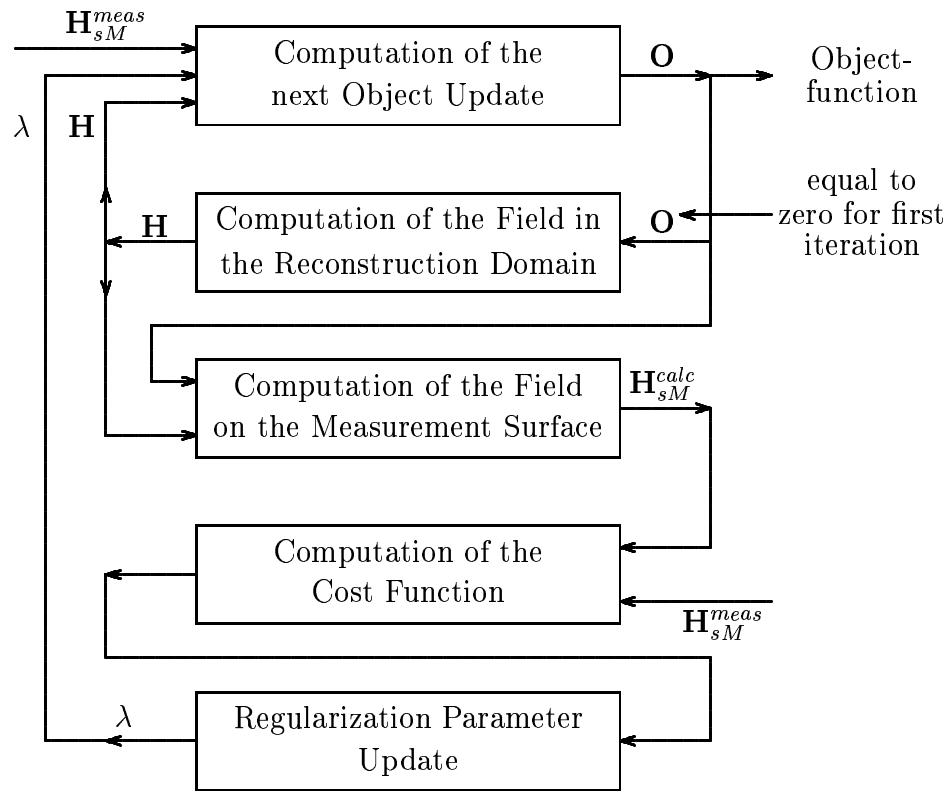


Fig. 4.

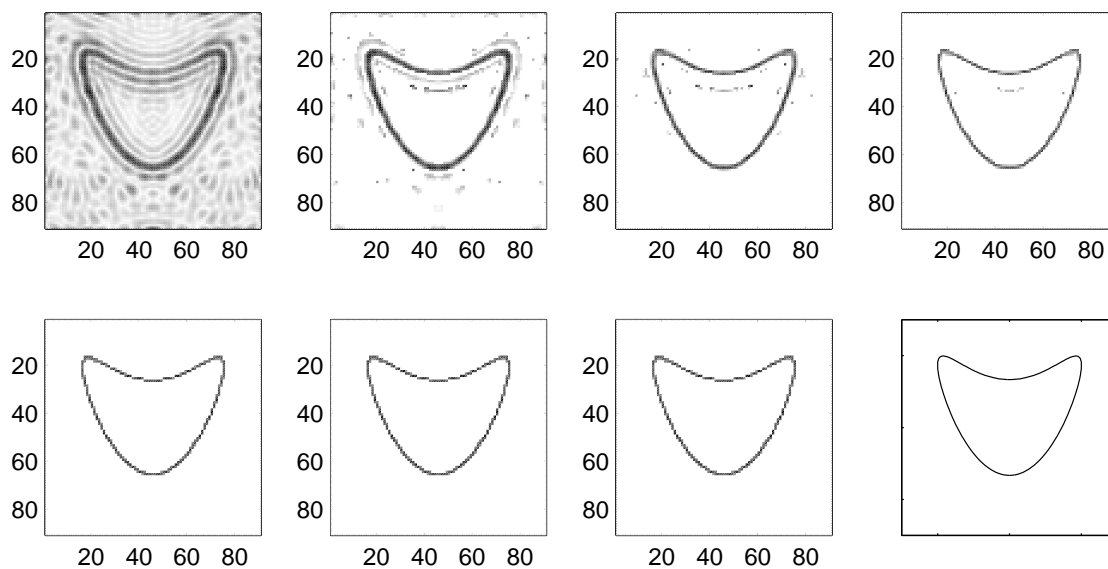


Fig. 5.

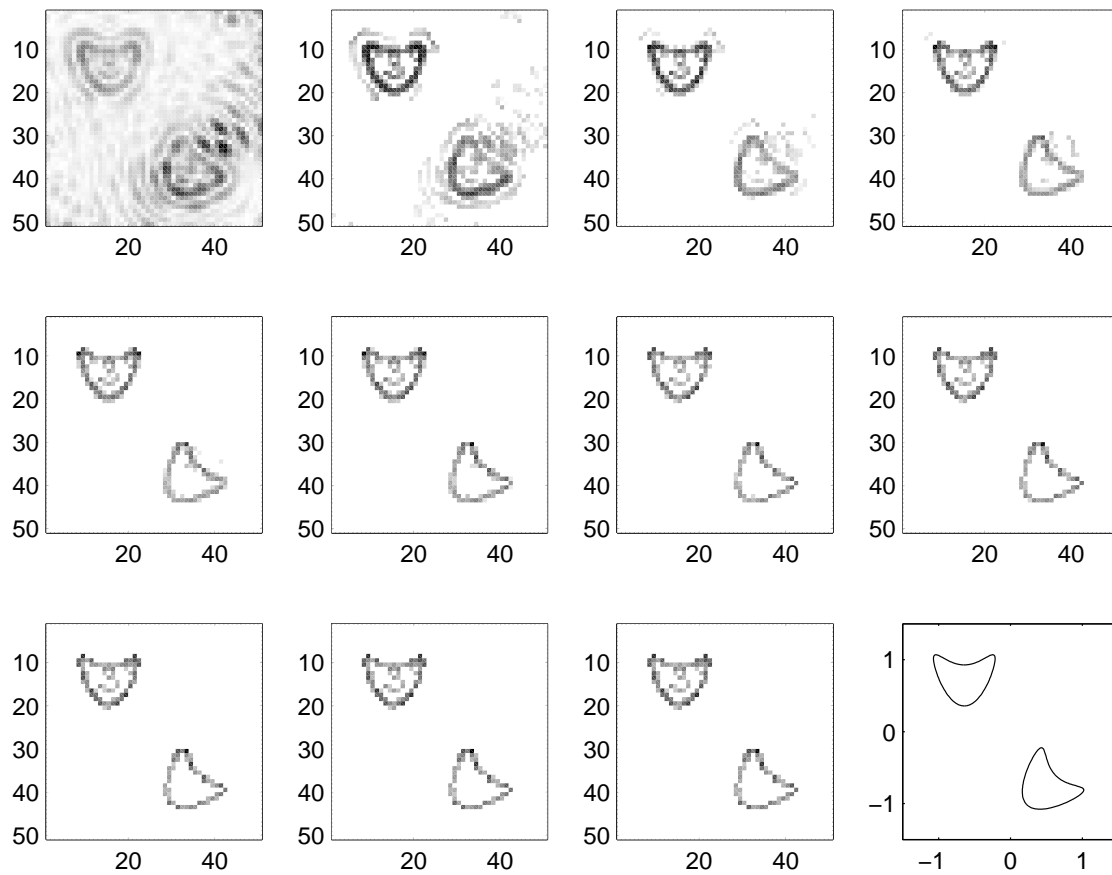


Fig. 6.

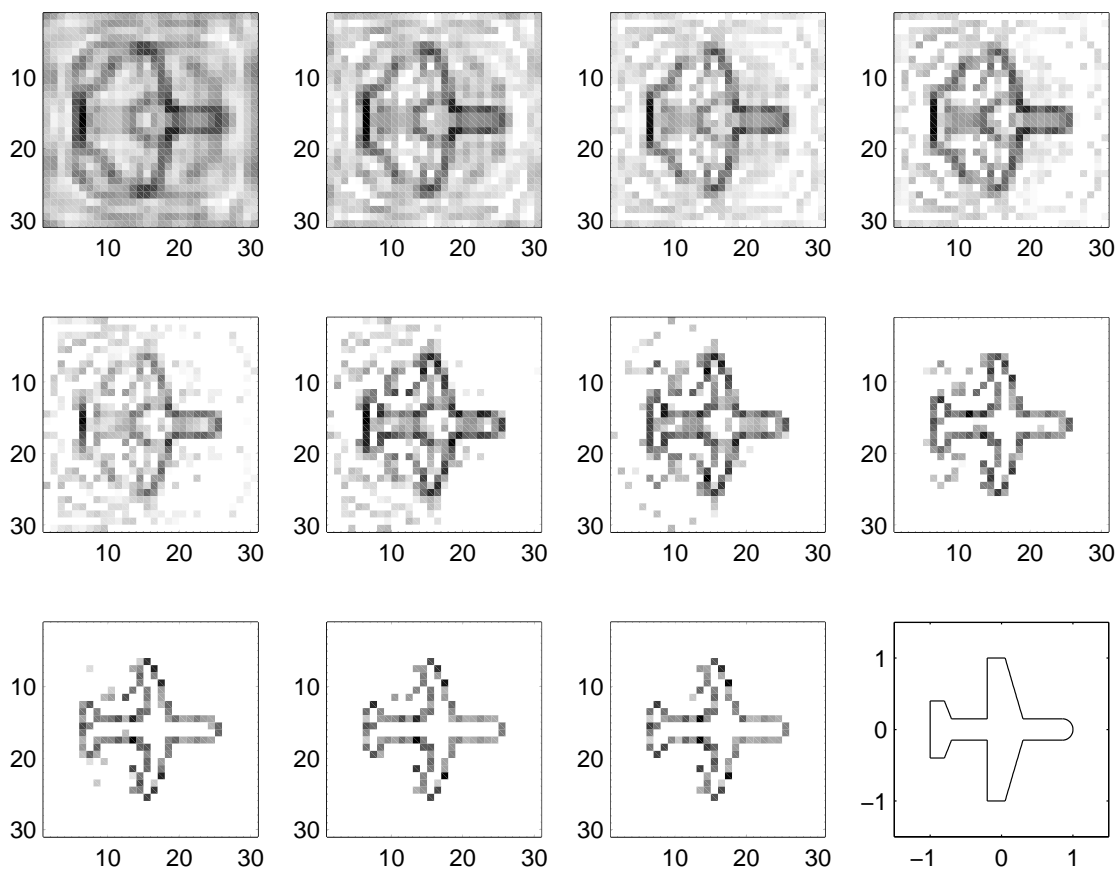


Fig. 7.

Fig. 1: FMM – interactions

Fig. 2: MLFMA – tree structure

Fig. 3: Three level Multilevel Fast Multipole Algorithm in two dimensions

Fig. 4: Iteration process of the DBIM

Fig. 5: Reconstruction of a ‘single kite’ with single-frequency excitation $k = 15.$, 32 incident sources around the reconstruction domain and 250 observation points on a circular measurement surface

Fig. 6: Reconstruction of a ‘double kite’ with single-frequency excitation $k = 7.6$, 16 incident sources around the reconstruction domain and 250 observation points on a circular measurement surface

Fig. 7: Reconstruction of an airplane model with multi-frequency excitation: 4 frequencies from $k_{min} = 1.5$ to $k_{max} = 9.2$ with 16 incident sources around the reconstruction domain and 250 observation points on a circular measurement surface